JOURNAL OF COLLOID AND INTERFACE SCIENCE **207,** 159–169 (1998)
ARTICLE NO. CS985748

# Pore Size Analysis of MCM-41 Type Adsorbents by Means of Nitrogen and Argon Adsorption[1]

Alexander V. Neimark,*,†,[2] Peter I. Ravikovitch,† Michael Grün,‡ Ferdi Schüth,§ and Klaus K. Unger‡

*TRI/Princeton, 601 Prospect Ave., Princeton, New Jersey 08542; †Department of Chemical Engineering, Yale University, 9 Hillhouse Ave., New Haven, Connecticut 06520; ‡Institut für Anorganische Chemie und Analytische Chemie, Johannes Gutenberg-Universität, Becherweg 24, D-55128 Mainz, Germany; and §Institut für Anorganische Chemie, Johann Wolfgang Goethe-Universität, M. Curie Str. 11, D-60439 Frankfurt/Main, Germany

Received May 26, 1998; accepted July 8, 1998

**Methods of nonlocal density functional theory (NLDFT), proposed recently for predictions of adsorption equilibrium and calculations of pore size distributions in micro- and mesoporous materials, were tested on reference MCM-41 materials. Five newly synthesized MCM-41 adsorbents with presumably uniform pore channels varying from 32 to 45 Å were characterized by X-ray diffraction (XRD), nitrogen adsorption at 77 K, and argon adsorption at 77 and 87 K. New sets of intermolecular interaction parameters of the NLDFT model for $N_2$ and Ar adsorption on MCM-41 were determined. The parameters were specified to reproduce the bulk liquid–gas equilibrium densities and pressures, liquid–gas interfacial tensions, and standard adsorption isotherms on nonporous surfaces in the multilayer adsorption region. The pore size distributions calculated from the desorption branches of the experimental isotherms measured at three different temperatures were consistent with each other. Comparison of the NLDFT-calculated pore sizes with XRD data showed that the thickness of pore walls in the MCM-41 samples under consideration varied from ca. 6 to 12 Å. We found no correlation between the pore size and the pore wall thickness. The results obtained support the NLDFT model as a suitable tool for characterizing nanoporous materials and predicting adsorption equilibrium. The MCM-41 samples studied can be used as references for adsorption measurements.** 

*Key Words:* **adsorption; density functional theory; capillary condensation; hysteresis; MCM-41; pore size distribution; isosteric heat.**

## INTRODUCTION

Nonlocal density functional theory (NLDFT) (1) is currently regarded as an adequate tool for predicting adsorption and calculating pore size distributions in micro- and mesoporous materials (2–6). It was shown that NLDFT qualitatively describes adsorption equilibrium and phase transitions in nanopores (3). However, so far, it has not been determined to what extent the NLDFT results are quantitatively correct. Testing of theoretical models is hampered mostly because of the lack of independent experimental data produced with well-characterized reference samples. To provide a required similarity to theoretical models, reference samples should contain uniform pores with the least geometrical heterogeneity.

Nanoporous adsorbents of the MCM-41 type (7, 8) are known to possess the most uniform hexagonal array of quasi-cylindrical pore channels as compared to other available porous materials and may serve as potential reference adsorbents (9). MCM-41 materials are currently under intense investigation with respect to their synthesis, modification, structure elucidation, and various potential applications as adsorbents, catalyst supports, and host systems for various purposes (10, 11). MCM-41 materials are synthesized following different reaction routes yielding products of gradated pore size, specific surface area, and well-defined morphology. Their structural properties can be controlled independently by physisorption, X-ray diffraction, high-resolution transmission electron microscopy, and size exclusion chromatography (11).

The major objectives of this paper are (a) to synthesize reference samples with uniform cylindrical pore channels of different sizes, (b) to characterize their structures using XRD and the adsorption of nitrogen at 77 K and argon at 77 and 87 K, (c) to determine and verify the intermolecular interaction parameters for the NLDFT model of $N_2$ and Ar adsorption, (d) to calculate the pore size distributions and pore wall thicknesses in the reference samples independently from different adsorption isotherms, and (e) to test the consistency of the NLDFT model developed.

## EXPERIMENTAL

Five MCM-41 samples with presumably uniform pore structure were prepared[3] and characterized by X-ray diffraction (XRD). XRD patterns (Fig. 1) of most of the samples exhibit four reflection peaks, which is consistent with the supposition

[1] This paper is an extended version of the paper presented at the 4th International Symposium on Characterization of Porous Solids (COPS-IV), Bath, UK, Sept 15–18, 1996.

[2] To whom correspondence should be addressed. E-mail: aneimark@triprinceton.org.

[3] One of these samples, C50, has been described in ref. 5. The details of the synthesis of the other samples will be presented elsewhere.



0021-9797/98 $25.00

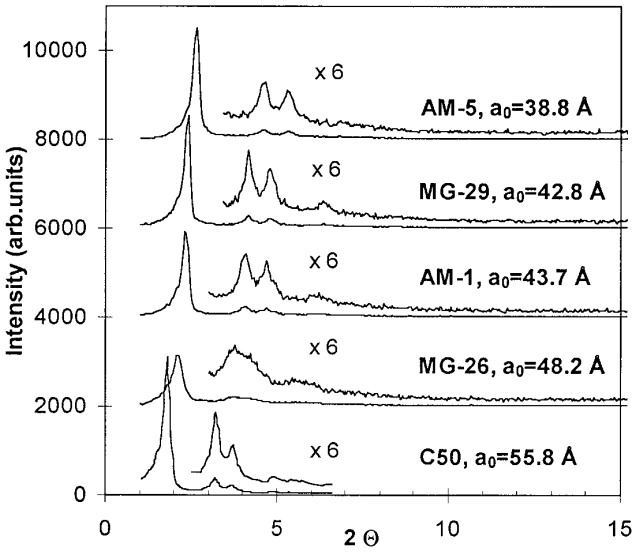


**FIG. 1.** X-ray diffraction patterns of MCM-41 samples.

that the pore channels form a regular hexagonal array. This allowed us to calculate the hexagonal unit cell parameter, $a_0 = 2d_{100}/\sqrt{3}$, the spacing between the centers of the adjacent pore channels. For an ideal, regular system the spacing is the sum of the internal pore diameter and the pore wall thickness.

Adsorption–desorption isotherms were measured volumetrically with the Autosorb-1-C instrument (Quantachrome Corp.) starting from the relative pressure of $P/P_0 \approx 1 \times 10^{-5}$. The isotherms are presented in Fig. 2. For Ar at 77.4 K the saturation pressure of the supercooled liquid Ar, $P_0 \approx 230$ Torr, was used. This choice is justified later. The vertical uptake at 77.4 K at $P/P_0 \approx 0.9$ corresponds to solidification of the bulk Ar. Due to the smaller size of the Ar molecule, Ar adsorption at both 77.4 and 87.3 K is greater than the $N_2$ adsorption.

Occurrence of the hysteresis loop depends on the adsorbate, pore size, and temperature. For the sample with the smallest pore size, neither $N_2$ nor Ar isotherms exhibit hysteresis (Fig. 2a). As the pore size increases, hysteresis appears first on Ar isotherms at 77 K (Figs. 2b and 2c), then on Ar isotherms at 87 K (Fig. 2d), and finally on $N_2$ isotherms (Fig. 2e). This is consistent with the lower reduced temperature ($T/T_c$) of Ar at 87 K compared to $N_2$ at 77 K and with the smaller size of the Ar molecule. Wider hysteresis loops are observed at lower reduced temperatures and/or larger pore sizes (12). The shape of the hysteresis loops varies from a "triangle" for the smaller size samples to a well-pronounced "parallelogram" of Type I according to the IUPAC classification (13). The only exception to this general rule was the Ar hysteresis loop at 77.4 K on the MG-26 sample (Fig. 2d), which was somewhat wider than the hysteresis loop on the C50 sample with larger pore sizes.

Comparative plots have been constructed versus the corresponding $N_2$ and Ar isotherms on a nonporous silica surface (13, 14). The comparative plots did not indicate any micropores (of size less than 2 nm) in all samples, in agreement with other studies (15).

From Ar isotherms measured at two temperatures, we have estimated the isosteric heats of adsorption (13):

$$q_{st} = \frac{RT_1T_2}{T_2 - T_1}(\ln P_2 - \ln P_1)_N. \qquad [1]$$

The coverage dependence of the isosteric heat (Fig. 3) is plotted versus the amount adsorbed normalized to Ar adsorption at 77 K and relative pressure $P/P_0 = 0.8$. All three samples exhibit a peak in the isosteric heat at a coverage of ca. $N/N_{0.8} \approx 0.95$, which is characteristic to capillary condensation. The isosteric heats increase as the pore size decreases due to the enhancement of solid–fluid interactions.

## NONLOCAL DENSITY FUNCTIONAL THEORY FOR $N_2$ AND Ar ADSORPTION ON MCM-41

### *NLDFT Model*

To predict both $N_2$ and Ar adsorption isotherms on MCM-41 samples, we use the NLDFT model, which has been developed earlier (5, 6) as applied to $N_2$ adsorption. The NLDFT model employed was described in detail in ref 5. A general scheme is as follows. The grand thermodynamic potential of a fluid confined in a pore at a given chemical potential $\mu$ and temperature $T$ is represented as a functional of the local fluid density $\rho(\mathbf{r})$:

$$\Omega[\rho(\mathbf{r})] = F[\rho(\mathbf{r})] - \int d\mathbf{r}\rho(\mathbf{r})[\mu - U_{ext}(\mathbf{r})], \qquad [2]$$

where $F[\rho(\mathbf{r})]$ is the intrinsic Helmholtz free energy functional and $U_{ext}(\mathbf{r})$ is the potential imposed by the pore walls. The Helmholtz free energy functional $F[\rho(\mathbf{r})]$ is divided into a contribution from the reference system of hard spheres, $F_{HS}[\rho(\mathbf{r})]$, for which we used the nonlocal density functional of Tarazona (16), which is proven to be an effective approximation for the problems of adsorption equilibrium in nanoconfinements (1–6). Contribution from attractive interactions is treated in a mean-field approximation:

$$F[\rho(\mathbf{r})] = F_{HS}[\rho(\mathbf{r})] + \frac{1}{2}\int\int d\mathbf{r}d\mathbf{r}'\rho(\mathbf{r})\rho(\mathbf{r}')\Phi_{attr}(|\mathbf{r} - \mathbf{r}'|). \qquad [3]$$

The attractive interactions, $\Phi_{attr}(r)$, are modeled as the Lennard-Jones potential using the Weeks–Chandler–Anderson (WCA) prescription for the division of the potential (17). The potential is truncated at a distance of 5 molecular diameters to

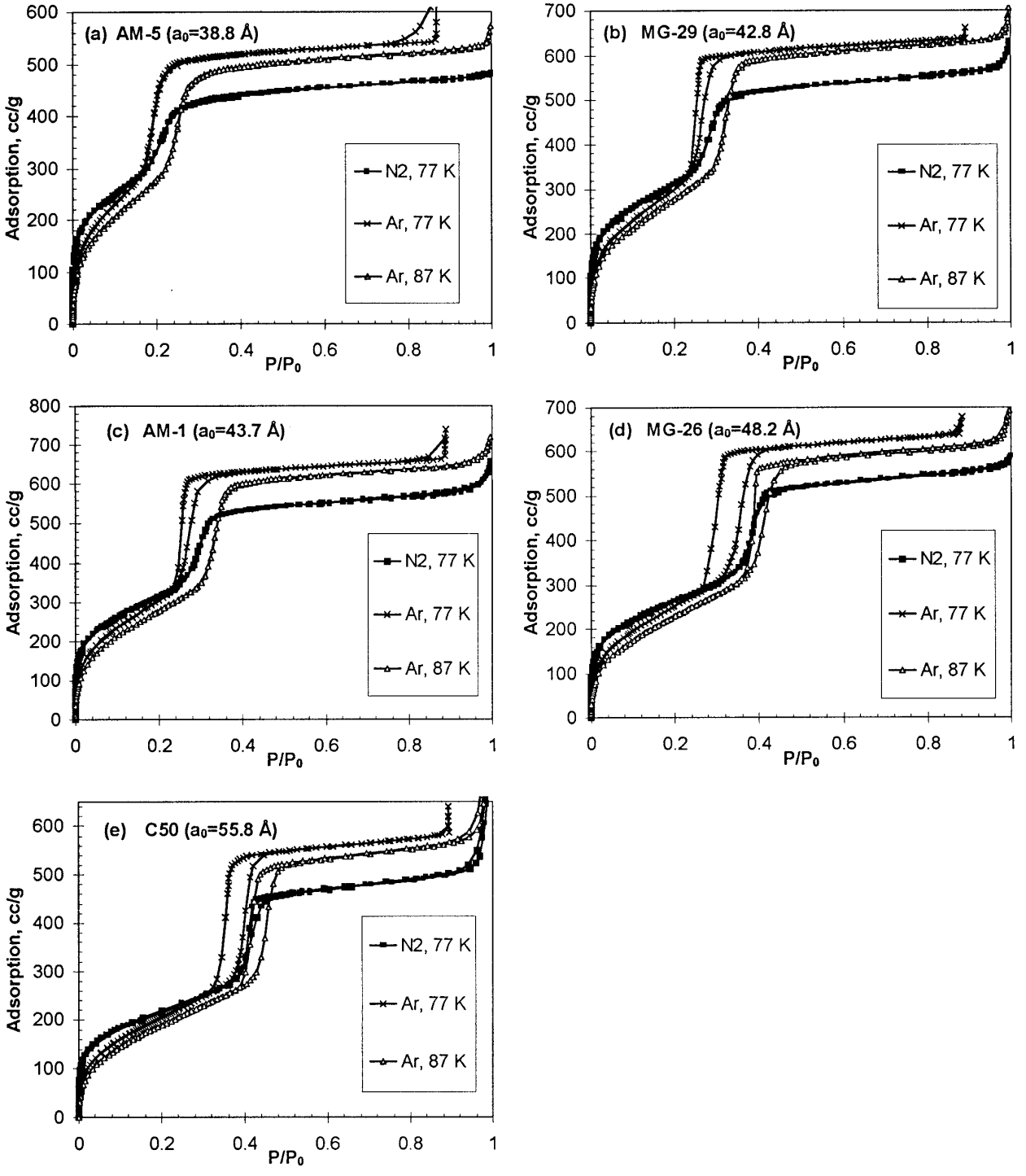


**FIG. 2.** Experimental adsorption isotherms of $N_2$ at 77.4 K and Ar at 77.4 and 87.3 K on MCM-41 samples. For Ar at 77.4 K, the saturation pressure of the supercooled liquid Ar was used.

reduce computational efforts in large pores. Properties of the bulk fluid are also calculated with the truncated potential.

Equilibrium density profiles are determined by minimization of the grand potential functional $\Omega[\rho(r)]$, Eq. [2], with respect to the local fluid density $\rho(\mathbf{r})$ by the method of the Indeterminate Lagrange Multipliers (ILM) (18). Adsorption isotherms in model cylindrical pores are calculated by integrating the density profiles along the radial coordinate:

$$N_V(\mu) = \frac{8}{(D - \sigma_{OO})^2} \int_0^{D/2} r\rho(r)dr - \rho_{bulk}(\mu). \quad [4]$$

Here $D$ is the pore diameter measured between the centers of the opposite layers of oxygen atoms in the pore wall, $\sigma_{OO} = 2.76$ Å is the diameter of oxygen atoms, $\rho_{bulk}$ is the equilibrium bulk gas density, and $N_V(\mu)$ is the excess adsorption expressed per unit of the *internal* volume of the pore.

The most important factor, which determines predicting capabilities of the model, is the choice of the parameters of the fluid–fluid and fluid–solid interactions. As most other authors (2, 4), we used the Lennard-Jones (LJ) approximation. However, the parameters were different from those published previously. The fluid–fluid interaction parameters were chosen to provide the most accurate fit to the experimental two-phase bulk equilibrium properties.

*Calculation of Bulk Properties*

In the mean-field DFT, the bulk fluid is described by the following equations of state:

$$\mu(\rho) = \mu_H(\rho) + 4\pi\rho \int_0^{r_c} r^2\Phi_{attr}(r)dr \quad [5]$$

$$P(\rho) = P_H(\rho) + 2\pi\rho^2 \int_0^{r_c} r^2\Phi_{attr}(r)dr, \quad [6]$$

where $\mu_H(\rho)$ and $P_H(\rho)$ are respectively the chemical potential and the pressure of the hard-sphere fluid calculated from the Carnahan–Starling equation (19); $r_c$ is the cut-off distance. The integral on the right-hand side of Eqs. [5] and [6] is equal to

$$4\pi \int_0^{r_c} r^2\Phi_{attr}(r)dr = -\alpha \frac{32}{9} \pi\epsilon_{ff}\sigma_{ff}^3 + \frac{16}{3} \pi\epsilon_{ff}\sigma_{ff}^3 \left[ \left(\frac{\sigma_{ff}}{r_c}\right)^3 - \frac{1}{3}\left(\frac{\sigma_{ff}}{r_c}\right)^9 \right], \quad [7]$$

where $\alpha = \sqrt{2}$ for the WCA division of the potential at $r = 2^{1/6}\sigma_{ff}$ (17) and $\alpha = 1$ when the potential is split according to the Barker–Henderson perturbation theory (20), i.e., at $r = \sigma_{ff}$. The first term on the right-hand side of Eq. [7] represents the integrated strength of attractive interactions for the infinitely long-range potential. The second term is a correction on the cut-off distance, which is quite small (but not negligible) for reasonably large cut-off distances ($r_c > 5\sigma_{ff}$), so that the mean-field equation of state is essentially a two-parameter equation which depends on the diameter of hard spheres, $d_{HS}$, and the product $\epsilon_{ff}\sigma_{ff}^3$.

We have tested two options for the choice of the hard-sphere diameter: (1) $d_{HS}$ constant at all temperatures and (2) $d_{HS}$ scaled with temperature according to the prescription of Verlet and Weis (2, 21, 22):

$$d_{HS} = \sigma_{ff} \frac{\eta_1 k_B T/\epsilon_{ff} + \eta_2}{\eta_3 k_B T/\epsilon_{ff} + \eta_4}. \quad [8]$$

Applicability of the mean-field equation of state to real fluids is generally limited to regions away from the critical point. For example, with the WCA prescription and $d_{HS} = \sigma_{ff}$ at all temperatures, the reduced critical temperature of the DFT model $T^* = k_B T/\epsilon_{ff} \approx 1.411$, which is higher than the critical temperature of the LJ fluid.

*Fluid–Fluid Interaction Parameters*

We did not attempt to fit the experimental phase diagrams of $N_2$ and Ar based on the critical temperature. Instead, the parameters of the LJ potentials were obtained by fitting the

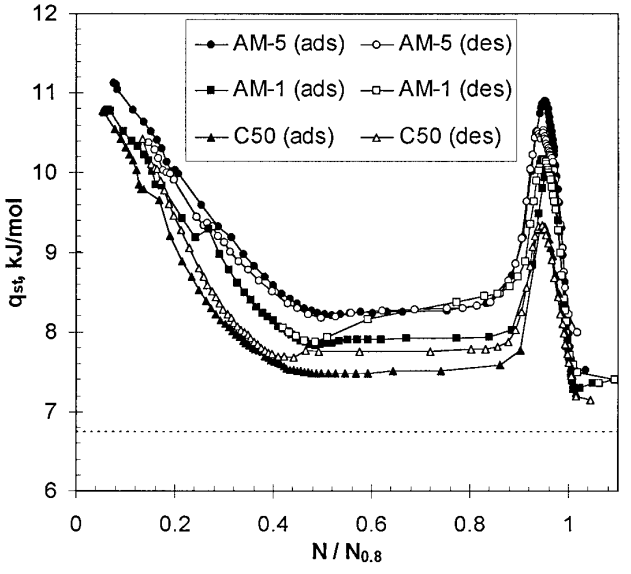


**FIG. 3.** Isosteric heats of Ar adsorption calculated from the experimental isotherms at 77.4 and 87.3 K. Molar heat of bulk condensation is shown by the dashed line.

**TABLE 1**
**Parameters of the NLDFT Model of Adsorption on MCM-41**

| | Fluid–fluid | | | Solid–fluid | |
|---|---|---|---|---|---|
| Adsorbate | $\epsilon_{ff}/k_B$ (K) | $\sigma_{ff}$ (Å) | $d_{HS}$ (Å) | $\rho\epsilon_{sf}/k_B$ (K/Å$^2$) | $\sigma_{sf}$ (Å) |
| $N_2$ | 94.45 | 3.575 | 3.575 | 22.53 | 3.17 |
| Ar | 118.05 | 3.305 | 3.38 | 26.2 | 3.0 |

*Note:* $\rho$ is the surface number density of oxygen atoms in the pore wall. Fluid–fluid interactions are truncated at $5\sigma_{ff}$.

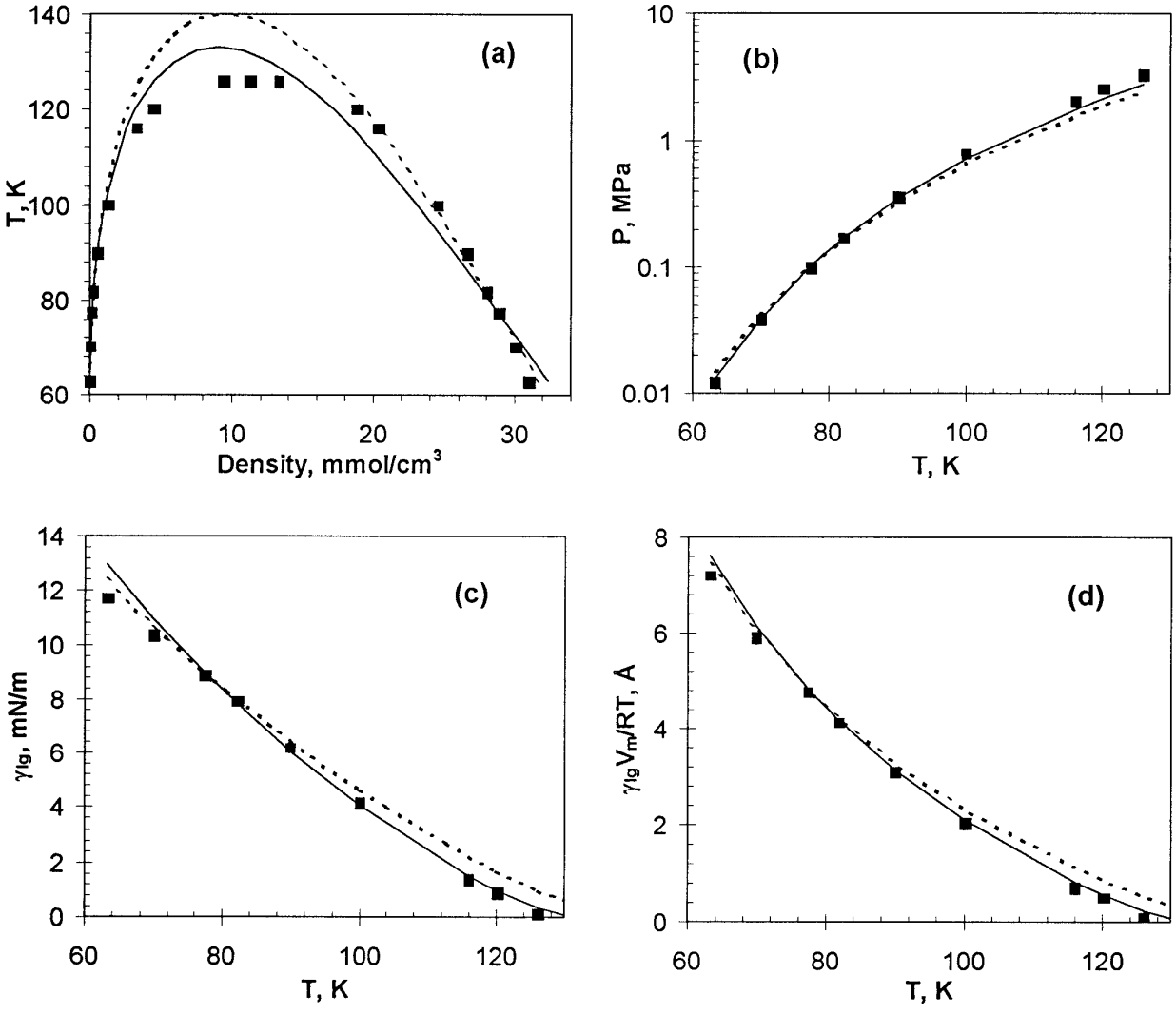


**FIG. 4.** Bulk equilibrium for nitrogen (critical point 126.2 K, triple point 63.15 K): (a) liquid–gas densities; (b) saturation pressure; (c) surface tension; (d) length parameter of the Kelvin equation. Experimental data (23, 26) (points); DFT calculations using constant hard-sphere diameter $d_{HS} = \sigma_{ff}$ (solid line); DFT calculations using temperature-dependent (Eq. [8]) hard-sphere diameter (dashed line). Parameters of Eq. [8] were $\eta_1 = 0.3837$, $\eta_3 = 0.4249$, $\eta_4 = 1$ (ref 2), and $\eta_2 = 1.034$ (ref 5).

experimental bulk properties taken from refs 23–25 within a diapason of temperatures, which included the temperatures of adsorption measurements (normal boiling points of both adsorbates). Parameters of the fluid–fluid interactions are listed in Table 1.

*Bulk Phase Diagrams*

In Figs. 4 and 5 we present calculated bulk phase diagrams of $N_2$ and Ar in comparison with experimental data. For $N_2$ (Figs. 4a and 4b), the liquid–gas coexistence densities and the saturation pressure agree to within 1% with the experimental values at 77.4 K. Both choices of the hard-sphere diameter provide a good description of bulk properties around the boiling point. As compared with the constant hard-sphere diameter approximation, the use of the temperature-dependent hard-sphere diameter [8] gives a better agreement with the experimental liquid branch and a worse agreement with the gas branch and with the saturation pressure curve (Figs. 4a and 4b). Also, the critical temperature of the model is shifted further away from the experimental value.

For Ar (Figs. 5a and 5b), the experimental liquid–gas coexistence densities are predicted with an accuracy better than 1% in the temperature range 83–90 K and with accuracy better than 5% at temperatures up to 105 K. The saturation pressure is predicted with accuracy better than 2% up to 125 K. The use of the temperature-dependent hard-sphere diameter has an effect similar to that for nitrogen. It significantly improves the liquid branch at higher temperatures. For Ar at low temperatures (below the boiling point), the difference between the two choices of the hard-sphere diameter is insignificant, and both of

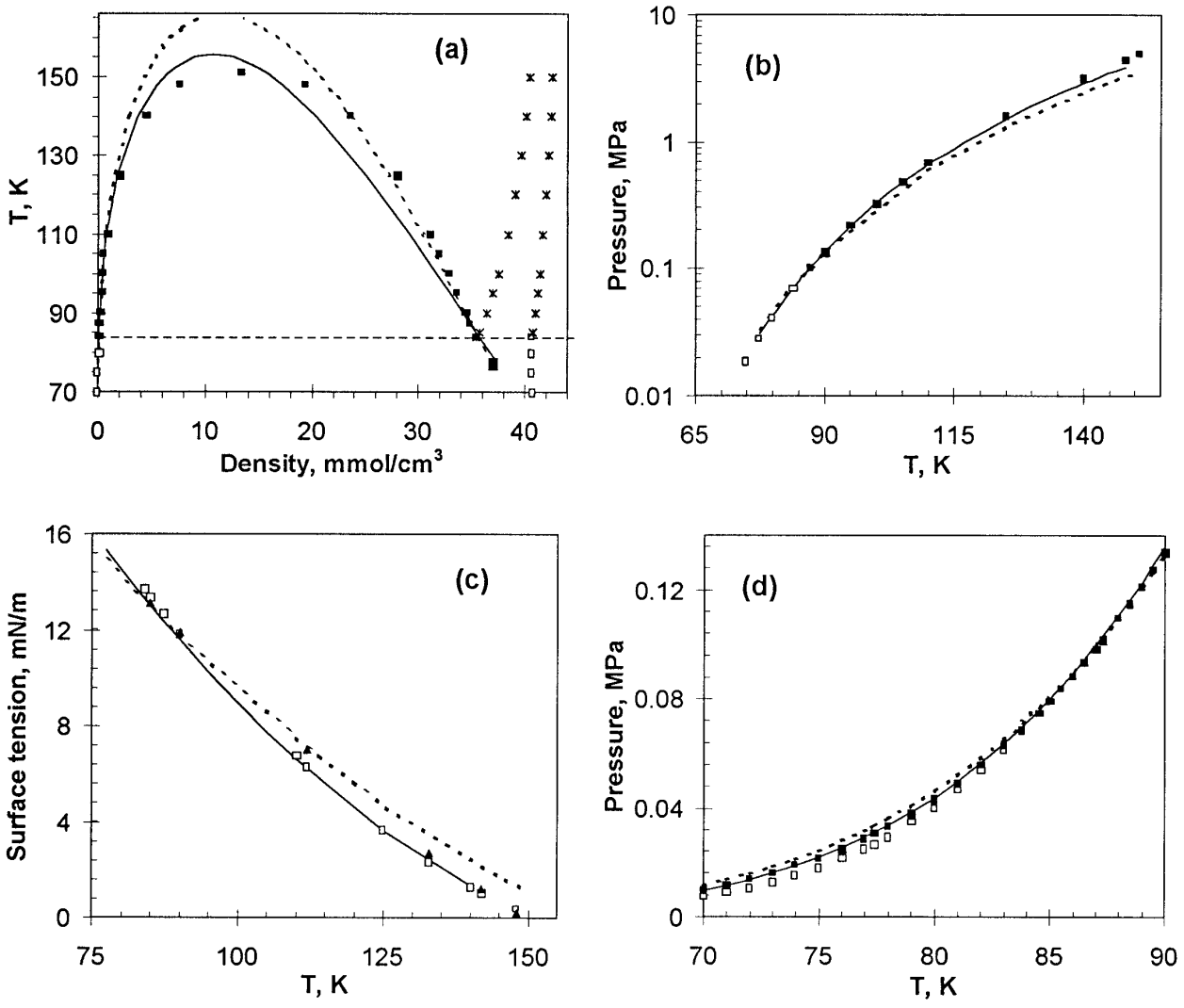


**FIG. 5.** Bulk equilibrium for argon [critical point 150.86 K, triple point 83.78 K (horizontal line in (a))]: (a) phase diagram [liquid–gas coexistence (black squares), liquid–solid line (stars), solid–gas line (open squares) (24)]; (b) saturation pressure [liquid–gas (black squares), solid–gas (open squares) (24)]; (c) surface tension [data from ref 26 (open squares), data from ref 27 (triangles)]; (d) vapor pressure [extrapolated experimental liquid branch (black squares) (ref 25), experimental solid–gas branch (open squares) (ref 25)]. For all plots: DFT calculations using constant hard-sphere diameter $d_{HS} = 1.0227\ \sigma_{ff} = 3.38$ Å (solid line), DFT calculations using temperature-dependent (Eq. [8]) hard-sphere diameter (dashed line). Parameters of Eq. [8] were $\eta_1 = 0.3837$, $\eta_3 = 0.4249$, $\eta_4 = 1$ (ref 2), and $\eta_2 = 1.0599$ (this work).

them give a reasonable description of the phase diagram in the region of interest (77–90 K).

*Liquid–Gas Surface Tension*

Another important factor is the liquid–gas surface tension. Correct prediction of the surface tension is a necessary condition for any model claiming quantitative description of the capillary condensation–desorption transition in pores. To predict the liquid–gas surface tension, we used the same NLDFT computation module which we employ for calculations of adsorption isotherms in pores. We calculated the equilibrium density profiles at the liquid–gas interface in planar symmetry using a box of $H \approx (30–60)\sigma_{ff}$ width. The surface tension was calculated as the excess grand potential of the system:

$$\gamma_{lg} = \Omega/S + P_{bulk}H, \qquad [9]$$

where $P_{bulk}$ is the equilibrium bulk pressure. The calculated surface tension of nitrogen at 77.4 K is only 1.5% greater than the experimental value (Fig. 4c, Table 1). Surprisingly, the agreement with the experimental data (26) is good even for temperatures close to the critical temperature. The use of the temperature-dependent hard-sphere diameter improves predictions of the surface tension at temperatures below the boiling point but worsens the agreement at higher temperatures. For Ar, the calculated surface tension agrees with both sets of the experimental data (26, 27) to within 2.5% in the temperature range 83–90 K (Fig. 5c).

For description of the capillary condensation transition in pores, the relevant parameter is $\gamma_{lg}V_m/RT$, i.e., the length

**TABLE 2**
**Bulk Liquid–Gas Equilibrium of $N_2$ at 77.4 K Calculated Using Different Parameters for the LJ Potential**

| $\sigma_{ff}$ (Å) | $\epsilon_{ff}/k_B$ (K) | Ref | Deviation in the gas density (%) | Deviation in the liquid density (%) | Deviation in the saturation pressure (%) | Surface tension (mN/m) | Deviation in the surface tension (%) |
|---|---|---|---|---|---|---|---|
| | | 13 | | | | 8.88 | |
| 3.75 | 95.2 | 28 | −24 | −12.5 | −23 | 9.1 | 2.5 |
| 3.694 | 96.26 | 29 | −28 | −8 | −27 | 9.8 | 10 |
| 3.613 | 103 | 30 | −57 | 2.7 | −56 | 12.5 | 41 |
| 3.632 | 104.2 | 31 | −62 | 1.7 | −61 | 12.8 | 44 |
| 3.99 | 95 | 32 | −36 | −27 | −35 | 8.1 | −8.8 |
| 3.572 | 93.98 | 2[a] | −1 | <0.2 | <0.2 | 9.6 | 8.1 |
| 3.5746 | 93.746 | 4 | −1 | <0.2 | <0.2 | 9.7 | 9.2 |
| 3.575 | 94.45 | 5[b] | <0.2 | <0.2 | 0.9 | 9.0 | 1.5 |
| | | This work | | | | | |

*Note.* WCA prescription for the attractive potential (ref 17); diameter of hard spheres, $d_{HS}$, is equal to $\sigma_{ff}$ (except for ref 2), full LJ potential (except for ref 5).
[a] $d_{HS}$ = 3.5749 Å.
[b] Cut-off distance $5\sigma_{ff}$.

factor appearing in the Kelvin equation ($V_m$ is the molar volume of liquid). The calculated values for nitrogen (Fig. 4d) are within 4% of the experimental data in the temperature range 70–90 K (ca. 1.5% at 77.4 K), and we expect that the model quantitatively predicts capillary condensation transitions in pores.

The intermolecular potential parameters used in this work differ from the LJ parameters of $N_2$ and Ar presented in the literature earlier. In Table 2 we compare predictions for the liquid–gas equilibrium of $N_2$ at 77 K calculated by using different sets of parameters taken from the literature. It is worth noticing that the deviations in the surface tension, calculated by using the best two sets of parameters (2, 4), were 8–9% despite the fact that these parameters give correct prediction of the liquid–gas densities and the saturation pressure.

Parameters of Ar used in this work ($\epsilon_{ff}/k_B$ = 118.05 K, $\sigma_{ff}$ = 3.305 Å) differ slightly from the most frequently used parameters of LJ Ar ($\epsilon_{ff}/k_B$ = 119.8 K, $\sigma_{ff}$ = 3.405 Å) (28). However, with the latter set of parameters the DFT model predicts at 87 K the gas density and saturation pressure, which are ca. 50% smaller than the experimental values, and the surface tension, which is 36% larger than the experimental value.

*Decomposition of Intermolecular Potentials*

We have also tested different prescriptions for dividing the intermolecular potential into the repulsive and attractive contributions. With the Barker–Henderson decomposition (20), the mean-field equation of state is unable to describe Ar bulk fluid at low temperatures with an acceptable accuracy. With the BH prescription, the reduced critical temperature is lower than the LJ fluid critical temperature. With the decomposition scheme proposed by Bruno *et al.* (33) and an appropriate set of parameters, the bulk fluid properties can be predicted with almost the same accuracy as in the case of the WCA decomposition. However, Bruno's prescription overestimates the role of attractive interactions, which leads to severe underestimation of the transition pressures in the pore fluid. This conclusion follows from the comparison of the theoretical isotherms with the experimental isotherms on well-characterized MCM-41 samples, for which the average pore size can be evaluated from X-ray diffraction. Thus, the WCA prescription for the attractive part of the intermolecular potential yields the most realistic results.

*Solid–Fluid Interaction Parameters*

The solid–fluid interactions in pores of MCM-41 materials were modeled as the Lennard-Jones interactions with the smooth cylindrical layer of oxygen atoms (5, 34). Parameters of the solid–fluid potential (Table 1) were chosen to fit the standard nitrogen and argon isotherms on nonporous solids in the multilayer adsorption region (for details, see ref 35). The distance parameters, $\sigma_{sf}$, for both $N_2$ and Ar are close to those calculated from the combining rule. The potential of the solid–fluid interactions used in this work (34) depends on the product $\rho_S\epsilon_{sf}$, where $\rho_S$is the effective surface number density of the oxygen atoms in the pore wall. We note that the parameters of the solid–fluid interactions for nitrogen differ slightly from the parameters employed in our earlier work (5). The new set of parameters gives better agreement with the standard nitrogen adsorption isotherm (35). The influence of the solid–fluid parameters on the predictions of the capillary condensation transition is discussed elsewhere (36). The main conclusion is that in the nanometer-size pores, typical for MCM-41, the fluid–fluid interaction parameters play a crucial role in determining the capillary condensation pressure, while the solid–fluid interactions can be effectively taken into account by using a simple homogeneous potential model.

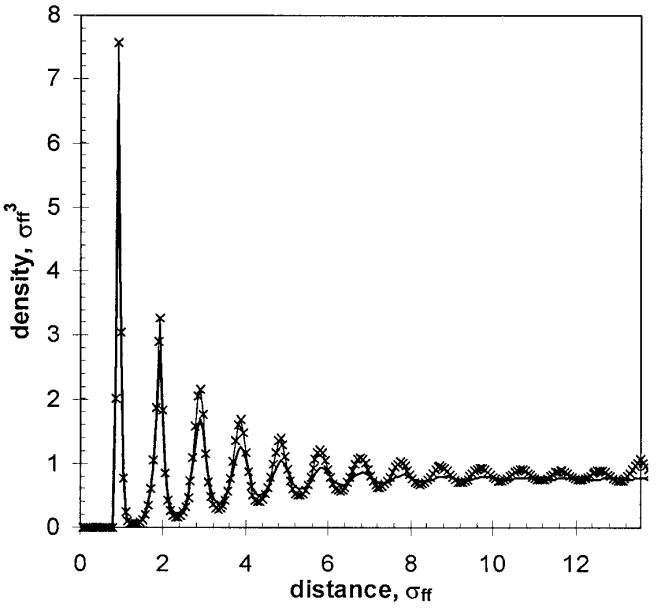


**FIG. 6.** Density profiles of Ar in a $27.1\sigma_{ff}$ cylindrical pore at 87.3 K (solid line) and at 77.4 K (crosses). The hard-sphere diameter $d_{HS}$ $1.023\sigma_{ff} = 3.38$ Å.

*Choice of the Ar Saturation Pressure at 77 K*

To construct the adsorption isotherm as a function of relative pressure $P/P_0$, we have to choose the value of the saturation pressure $P_0$. In the case of Ar at the $N_2$ boiling temperature 77.4 K, which is below the triple point of bulk Ar (83.8 K), this choice is not uniquely defined. Two different values for the saturation pressure, which correspond to the solid and to the supercooled liquid, are used in the adsorption literature (13). Equations [5] and [6] describe only a homogeneous fluid and thus do not predict the bulk solid–gas coexistence line (37). However, the calculated liquid density and saturation pressure of Ar fluid at 77.4 K reproduce well the density and saturation pressure of the supercooled liquid Ar (25). The latter is obtained by extrapolating the experimental liquid–gas saturation pressures (25) below the triple point (Fig. 5d). At 77.4 K, the saturation pressure of the supercooled Ar is 229.1 Torr (25). The calculated value is 231.8 Torr. Therefore, to compare theoretical and experimental Ar isotherms at 77.4 K, the saturation pressure of the supercooled liquid Ar was used instead of the experimentally measured saturation pressure of solid Ar (ca. 205 Torr).

This choice is supported by the NLDFT predictions of the liquid-like structure of Ar in pores. In Fig. 6 we present calculated density profiles of Ar in a relatively wide mesopore of $27.1\sigma_{ff}$ (internal diameter 86.8 Å) at two temperatures, above and below the experimental triple point. Both profiles exhibit pronounced layering near the pore wall. Oscillations at higher temperature (87.3 K) have smaller amplitudes as compared to those at lower temperature (77.4 K) and decay to the bulk liquid density at ca. $8\sigma_{ff}$ apart from the wall. At 77.4 K, some layering persists even in the middle of the pore; however, the average density is equal to the bulk liquid density.

## CALCULATION OF THE PORE SIZE DISTRIBUTIONS

To calculate the pore size distributions, the experimental isotherm is described as a superposition of isotherms in individual pores. This is a well-justified assumption for materials of the MCM-41 type:

$$N_{exp}(P/P_0) = \int_{D_{min}}^{D_{max}} \varphi(D_{in})\, N_V(D_{in}, P/P_0)\, dD_{in}, \qquad [10]$$

where $N_{exp}(P/P_0)$ is the experimental isotherm, $N_V(D_{in}, P/P_0)$ is the theoretical isotherm in pores of size $D_{in} = D - \sigma_{OO}$, and $\varphi(D_{in})$ is the pore size distribution. Three sets of theoretical isotherms have been calculated: $N_2$ at 77.4 K, Ar at 77.4, and Ar at 87.3 K. The range of pore sizes varied from 18 to 80 Å. When constructing the kernel of the integral equation [10], we took advantage of the fact that experimental isotherms on MCM-41 in the multilayer adsorption region are similar to corresponding isotherms on nonporous surfaces (15). The latter were used to represent kernel isotherms in this region (15). This procedure does not affect the calculated pore size distribution but simplifies the solution of Eq. [10] by eliminating the pronounced layering seen on the theoretical isotherms which arises from the homogeneous potential of solid–fluid interactions used in this model (5).

Integral equation [10] has been discretized using the trapezoidal rule of integration and solved by using the standard Tikhonov regularization method, which minimizes the 2-norm of the solution vector (38). This procedure involved the singular value decomposition (SVD) of the kernel matrix.

In Fig. 7 we present the pore size distributions of MCM-41 samples calculated from $N_2$ isotherms at 77 K and Ar isotherms at 77 and 87 K. The pore size distributions for the AM-5, MG-29, C50, and AM-1 samples, calculated from the Ar isotherms at two temperatures, are almost identical and coincide well with the distribution obtained from the $N_2$ isotherm at 77 K. This indicates the NLDFT model consistency. We note that for the samples which exhibit hysteretic isotherms (MG-29, AM-1, and C50), a good agreement between the calculated pore size distributions was obtained by using the desorption branches of the experimental isotherms rather than the adsorption branches. For comparison, we also included the pore size distributions calculated from the adsorption branches of Ar isotherms at 77 K. These distributions deviate appreciably from the distributions obtained from Ar isotherms at 87 K and from $N_2$ isotherms at 77 K (Figs. 7b, 7c, and 7e), especially for the C50 sample (Fig. 7e), which exhibits the most prominent hysteretic isotherms. This supports our earlier conclusion (5, 6) that the desorption branch of isotherms in cylindrical pores of MCM-41 corresponds to equilibrium transitions and should be employed in the pore size analysis.

One of the samples used in this work (MG-26) seems to be somewhat exceptional. For this sample, the agreement between

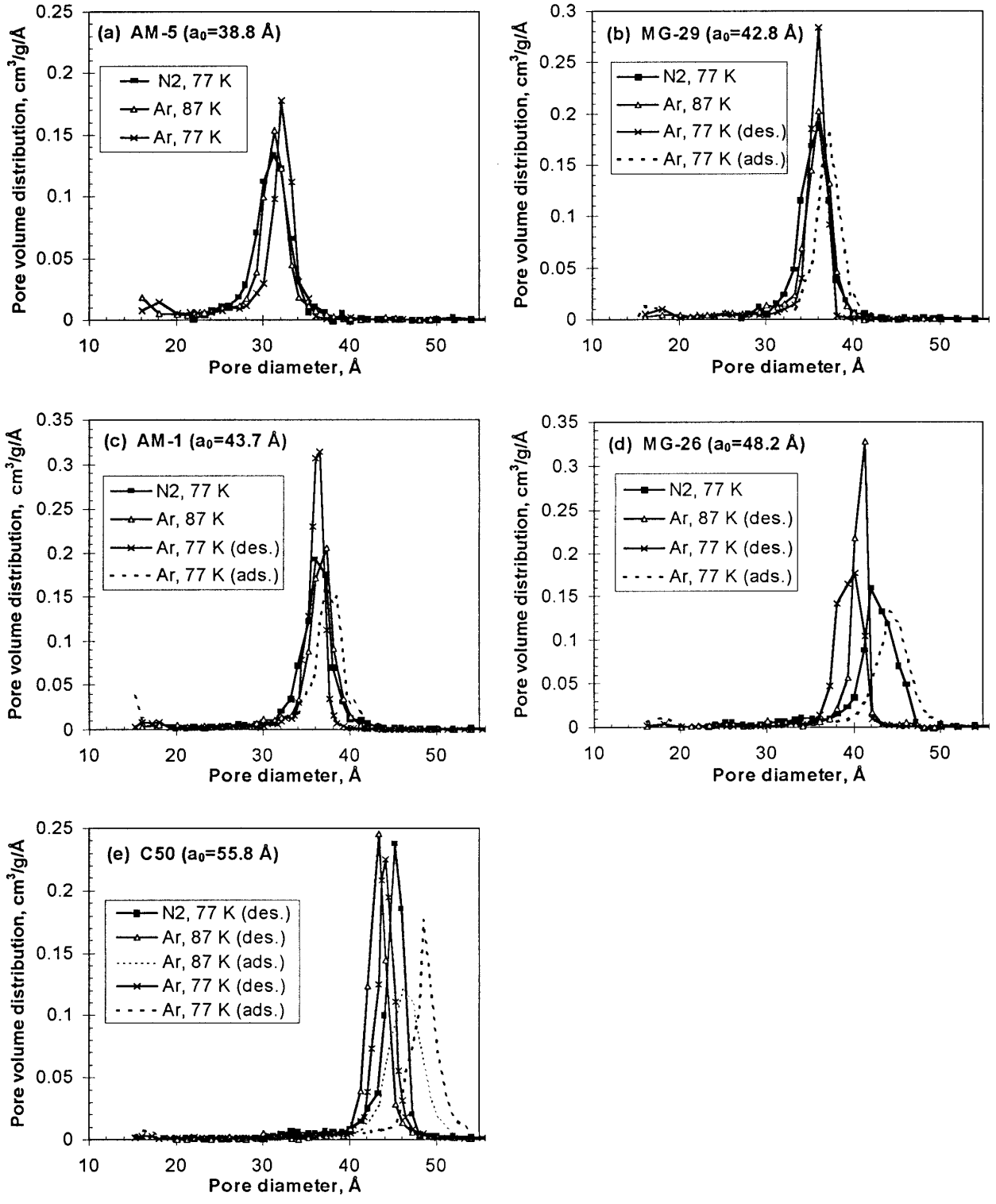


**FIG. 7.** Pore size distributions calculated from the NLDFT model: calculated from the desorption branches (solid lines); calculated from the adsorption branches (dashed lines).

the pore size distributions calculated from $N_2$ and Ar isotherms is worse than for the four other samples (Fig. 7d). We note, however, that this is the only sample whose X-ray diffraction pattern (Fig. 1) did not exhibit distinct (110) and (200) peaks, and thus the structure cannot be considered as ideally hexagonal. Also, we mentioned earlier that the Ar hysteresis loop at

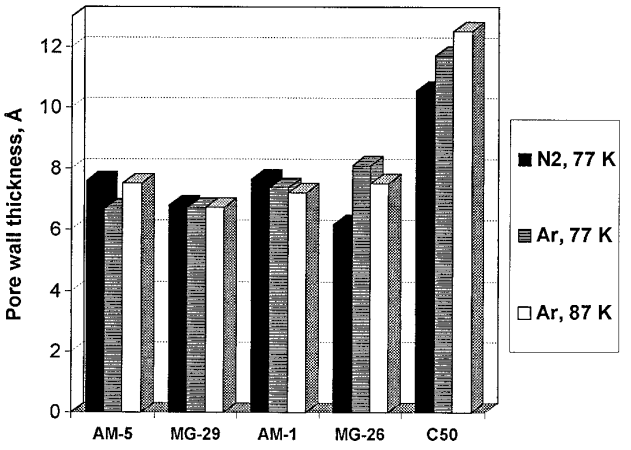


**FIG. 8.** Pore wall thickness calculated from the NLDFT model and XRD data.

77 K on this sample was wider than expected (Fig. 2d), which is likely related to a nonuniformity of pore channels. Despite these discrepancies, the pore size distributions calculated from the desorption branches of the isotherms are still closer to each other as compared to the pore size distribution calculated from the adsorption branch of the Ar isotherm at 77 K (Fig. 7d).

The thickness of the pore walls of the MCM-41 samples was calculated by subtracting the internal pore size from the spacing between pores, $a_0$, obtained from XRD. The results are shown in Fig. 8. The pore wall thickness of four out of five samples varied from ca. 6 to 8 Å. Larger pore wall thickness was obtained for the widest pore sample C50 (10–12 Å). Our analysis does not show a correlation between the average pore size of MCM-41 and the pore wall thickness. The pore wall thicknesses obtained by the NLDFT method agree reasonably with other independent estimates for the wall thickness in MCM-41 and similar materials (8, 39–41), in particular with the pore wall thickness obtained from transmission electron microscopy (39, 40). For comparison, the pore wall thickness of MCM-41 materials calculated from the conventional methods of pore size analysis, such as the Barrett–Joyner–Halenda (BJH) method (13), is usually unrealistically large (15). This is because the BJH method underestimates the pore size by ca. 10 Å for pores in the range 20–40 Å, as compared to the NLDFT model (5, 15, 35).

## CONCLUSIONS

We have tested the NLDFT model against low-temperature $N_2$ and Ar adsorption isotherms on reference MCM-41 materials with pore sizes varying from 32 to 45 Å. New sets of intermolecular potential parameters for $N_2$ and Ar were determined. The fluid–fluid interaction parameters were specified to reproduce the thermodynamic properties of the bulk fluid at low temperatures, including the liquid–gas surface tension. The parameters obtained differ from those presented in the literature earlier. The solid–fluid interaction parameters were found from the fit to the standard isotherm on the nonporous surface. We have demonstrated that the NLDFT model gives consistent results with respect to the pore size distributions and pore wall thicknesses. The pore size distributions calculated from $N_2$ isotherms at 77 K and from Ar isotherms at 77 and 87 K were in good agreement, provided that desorption branches of the experimental isotherms were employed. The pore wall thicknesses of reference MCM-41 samples, calculated by combining the pore size analysis with the XRD data, were in the range 6–12 Å. This agrees reasonably with other independent estimates. For MCM-41 materials used in this work, we found no definite correlation between the pore size and the pore wall thickness.

In summary, the NLDFT model represents a consistent approach, which can be recommended for quantitative predictions of adsorption equilibria in nanopores and calculations of pore size distributions in nanoporous materials from low-temperature $N_2$ and Ar isotherms.

## ACKNOWLEDGMENTS

The authors thank Dr. S. C. Ó Domhnaill for the C50 sample, Dr. A. Matsumoto for the AM-1 and AM-5 samples, and Quantachrome Corp. for the free loan of the adsorption instrument.

## REFERENCES

1. Evans, R., *in* "Fundamentals of Inhomogeneous Fluids" (D. Henderson, Ed.), Chapter 5. Marcel Dekker, New York, 1992.
2. Lastoskie, C., Gubbins, K. E., and Quirke, N., *J. Phys. Chem.* **97,** 4786 (1993); *Langmuir* **9,** 2693 (1993).
3. Balbuena, P. B., and Gubbins, K. E., *Langmuir* **9,** 1801 (1993).
4. Olivier, J. P., *J. Porous Mater.* **2,** 217 (1995); Olivier, J. P., Conklin, W. B., and v. Szombathely, M., *in* "Characterization of Porous Solids III, Studies in Surface Science and Catalysis" (J. Rouquerol, F. Rodriguez-Reinoso, K. S. W. Sing, and K. K. Unger, Eds.), Vol. 87, p. 81. Elsevier, Amsterdam, 1994.
5. Ravikovitch, P. I., Ó Domhnaill, S. C., Neimark, A. V., Schüth, F., and Unger, K. K., *Langmuir* **11,** 4765 (1995).
6. Neimark, A. V., Ravikovitch, P. I., Ó Domhnaill, S. C., Schüth, F., and Unger, K. K., *in* "Fundamentals of Adsorption" (M. D. LeVan, Ed.), p. 667. Kluwer Academic Publishers, Boston, 1996.
7. Beck, J. S., Vartuli, J. C., Roth, W. J., Leonowicz, M. E., Kresge, C. T., Schmitt, K. D., Chu, C. T.-W., Olson, D. H., Sheppard, E. W., McCullen, S. B., Higgins, J. B., and Schlenker, J. L., *J. Am. Chem. Soc.* **114,** 10834 (1992).
8. Monnier, A., Schüth, F., Huo, Q., Kumar, D., Margolese, D., Maxwell, R. S., Stucky, G. D., Krishnamurty, M., Petroff, P., Firouzi, A., Janicke, M., and Chmelka, B. F., *Science* **261,** 1299 (1993).
9. Branton, P. J., Hall, P. G., Sing, K. S. W., Reichert, H., Schüth, F., and Unger, K. K., *J. Chem. Soc., Faraday Trans.* **90,** 2965 (1994).
10. Sayari, A., *in* "Recent Advances and New Horizons in Zeolite Science and Technology, Studies in Surface Science and Catalysis" (H. Chon, S. I. Woo, and S.-E. Park, Eds.), Vol. 102, Chapter 1. Elsevier, Amsterdam, 1996.
11. Ciesla, U., Gruen, M., Isajeva, T., Kurganov, A. A., Neimark, A. V., Ravikovitch, P., Schacht, S., Schüth, F., and Unger, K. K., *in* "Access in Nanoporous Materials" (T. J. Pinnavaia and M. F. Thorpe, Eds.), p. 231. Plenum Press, New York, 1995.

12. Evans, R., Marini Bettolo Marconi, U., and Tarazona, P., *J. Chem. Soc., Faraday Trans. 2* **82,** 1763 (1986).
13. Gregg, S. J., and Sing, K. S. W., "Adsorption, Surface Area and Porosity." Academic Press, New York, 1982.
14. Gobet, J., and Kováts, E. sz., *Adsorp. Sci. Technol.* **1,** 111, 285 (1984).
15. Ravikovitch, P. I., Wei, D., Chueh, W. T., Haller, G. L., and Neimark, A. V., *J. Phys. Chem. B* **101,** 3671 (1997).
16. Tarazona, P., *Phys. Rev. A* **31,** 2672 (1985); *Phys. Rev. A* **32,** 3148 (1985).
17. Weeks, J. D., Chandler, D., and Andersen, H. C., *J. Chem. Phys.* **54,** 5237 (1971).
18. Neimark, A. V., *Langmuir* **11,** 4183 (1995).
19. Carnahan, N. F., and Starling, K. E., *J. Chem. Phys.* **51,** 635 (1969).
20. Barker, J. A., and Henderson, D., *J. Chem. Phys.* **47,** 4714 (1967).
21. Verlet, L., and Weis, J. J., *Phys. Rev. A* **5,** 939 (1972).
22. Lu, B. Q., Evans, R., and Telo da Gama, M. M., *Mol. Phys.* **55,** 1319 (1985).
23. "International Thermodynamic Tables of the Fluid State—6. Nitrogen" (S. Angus *et al.*, Eds.). Pergamon Press, Oxford, 1977.
24. "Encyclopedie des Gas—L'Air Liquide." Elsevier, Amsterdam, 1976.
25. Rabinovich, V. A., Vasserman, A. A., Nedostup, V. I., and Veksler, L. S., "Thermophysical Properties of Neon, Argon, Krypton, and Xenon." Hemisphere Publishing, Washington, DC, 1988.
26. Yaws, C. L., "Physical Properties." McGraw-Hill, New York, 1977.
27. McCormack, P. D., *Surf. Sci.* **26,** 375 (1971).
28. Hirschfelder, J. O., Curtiss, C. F., and Bird, R. B., "Molecular Theory of Gases and Liquids," 2nd ed. J. Wiley and Sons, New York, 1964.
29. Tee, L. S., Gotoh, S., and Stewart, W. E., *I&EC Fundam.* **5,** 356 (1966).
30. Clifford, A. A., Gray, P., and Platts, N., *J. Chem. Soc., Faraday Trans. 1* **73,** 381 (1977).
31. Rigby, M., Smith, E. B., Wakeham, W. A., and Maitland, G. C., "The Forces between Molecules." Clarendon Press, Oxford, 1986.
32. Bottani, E. J., and Bakaev, V. A., *Langmuir* **10,** 1550 (1994).
33. Bruno, E., Caccamo, C., and Tarazona, P., *Phys. Rev. A* **35,** 1210 (1987).
34. Tjatjopoulos, G. J., Feke, D. L., and Mann, J. A., Jr., *J. Phys. Chem.* **92,** 4006 (1988).
35. Ravikovitch, P. I., Haller, G. L., and Neimark, A. V., *Adv. Colloid Interface Sci.* **76-77,** 203 (1998).
36. Ravikovitch, P. I., Haller, G. L., and Neimark, A. V., *in* "Proceedings of the International Symposium on Mesoporous Molecular Sieves (Studies in Surface Science and Catalysis)," Vol. 117, p. 77. Elsevier, New York, 1998.
37. Tarazona, P., *Mol. Phys.* **52,** 81 (1984).
38. Lawson, C. L., and Hanson, R. J., "Solving Least Squares Problems." SIAM, Philadelphia, 1995.
39. Chen, C.-Y., Li, H.-X., and Davis, M. E., *Microporous Mater.* **2,** 17 (1993).
40. Chen, C.-Y., Xiao, S.-Q., and Davis, M. E., *Microporous Mater.* **4,** 1 (1995).
41. Inagaki, S., Sakamoto, Y., Fukushima, Y., and Terazaki, O., *Chem. Mater.* **8,** 2089 (1996).